# Computational Fluid Dynamics Analysis and Optimisation of Polymerase Chain Reaction Thermal Flow Systems

Hazim S. Hamad[a,b,*], N. Kapur[b], Z. Khatir[c], O.M. Querin[b], H.M. Thompson[b], Yongxing Wang[b], M.C.T. Wilson[b]

[a] *Ministry of oil, Iraq*
[b] *School of Mechanical Engineering, University of Leeds, Leeds, UK.*
[c] *Birmingham City University, UK.*

**Abstract**

A novel Computational Fluid Dynamics-enabled multi-objective optimisation methodology for Polymerase Chain Reaction flow systems is proposed and used to explore the effect of geometry, material and flow variables on the temperature uniformity, pressure drop and heating power requirements, in a prototype three-zone thermal flow system. A conjugate heat transfer model for the three-dimensional flow and heat transfer is developed and solved numerically using COMSOL Multiphysics® and the solutions obtained demonstrate how the design variables affect each of the three performance parameters. These show that choosing a substrate with high conductivity and small thickness, together with a small channel area, generally improves the temperature uniformity in each zone, while channel area and substrate conductivity have the key influences on pressure drop and heating power respectively. The multi-objective optimisation methodology employs accurate surrogate modelling facilitated by Machine Learning via fully-connected Neural Networks to create Pareto curves which demonstrate clearly the compromises that can be struck between temperature uniformity throughout the three zones and the pressure drop and heating power required.

*Keywords:* PCR, Computational Fluid Dynamics, Machine Learning, Multi-Objective Optimisation.

*Corresponding author
*Email address:* mnhsh@leeds.ac.uk (Hazim S. Hamad)

**Nomenclature**

| | |
|---|---|
| A | area ($m^2$) |
| $Bi$ | biot number |
| $C_p$ | constant-pressure specific heat |
| $D_h$ | hydraulic diameter ($mm$) |
| $H$ | microchannel height ($mm$) |
| $h^{'}$ | Heat transfer coefficient [$W/m^2.K$] |
| $k$ | thermal conductivity ($W/m.K$) |
| $L$ | length ($mm$) |
| $\dot{m}$ | mass flow rate ($kg/s$) |
| $N_u$ | Nusselt number |
| $P$ | microchannel perimeter ($mm$) |
| $\Delta p$ | pressure drop ($Pa$) |
| $Pe$ | Peclet number , $V_{ch}D_h/\alpha$ |
| $Pr$ | Prandtl number |
| $q$ | wall heat flux ($W/m^2$) |
| $Q$ | total power generated by PCR chip ($W$) |
| $R_{th}$ | conduction thermal resistance ($K/W$) |
| $Re$ | Reynolds number , $Re = \rho V_{ch}D_h/\mu$ |
| $S$ | spacing between heaters ($mm$) |
| $T$ | temperature ($K$) |
| $V$ | velocity ($mm/s$) |
| $\dot{V}$ | volumetric flow rate ($m^3/s$) |
| $W$ | width |

**Subscripts**

| | |
|---|---|
| $avg$ | average |
| $b$ | substrate |
| $c$ | channel |
| $CFD$ | computational fluid dynamics |
| $dev$ | deviation |
| $FEM$ | finite element method |
| $f$ | fluid |
| $h$ | heater |
| $in$ | inlet |
| $max$ | maximum |
| $min$ | minimum |
| $out$ | outlet |
| $RMSE$ | root-mean-square error |
| $s$ | solid |
| $w$ | wall |

**Greek symbols**



| | |
|---|---|
| $\alpha$ | thermal diffusivity |
| $\Delta$ | drop |
| $\rho$ | density ($kg/m^3$) |
| $\mu$ | dynamic viscosity ($Pa.s$) |
| $\nu$ | kinematic viscosity ($m^2/s$) |

## 1. Introduction

Precise thermal control during the processing of small volumes of liquid in arrays of fluidic channels is a key enabling technology for numerous important applications. These include chemical reactors, fuel and solar cells, pharmaceuticals and droplet freezing systems to determine environmental pollution levels [1, 2]. In the context of electronics cooling, the increasing densities of integrated circuits (up to $10kW/cm^2$ by 2020 [3]) have inspired significant recent research interest in single phase liquid flows in fluidic channels as a viable and practical method for cooling high heat flux densities encountered e.g. in Radio Frequency and microwave applications [4]. Serpentine fluidic channels are particularly useful. In addition to being capable of providing uniform processor temperatures for high density electronics cooling applications [5], they have found widespread application in the Polymerase Chain Reaction (PCR) systems that have revolutionised biological research [6].

This paper is motivated by the thermo-flow design and optimisation of fluidic channels used in PCR systems. They are used widely in rapid diagnostic systems for bacterial species leading to e.g. infectious diseases, or for the rapid and accurate detection of bacterial species causing micro-biologically induced corrosion in oil and gas production systems [7, 8]. PCR systems perform a thermal cycling procedure in a serpentine fluidic channel, where each straight component incorporates three distinct stages of denaturation (melting of the double-stranded DNA at $\sim 95°C$), annealing (binding of the specific primers of the thermo-stable DNA polymerase between $40°C \sim 50°C$) and extension (extending the primers within the thermo-stable DNA at $60°C \sim 70°C$) [9].

Early PCR systems used time-consuming devices involving wells where the whole chip is heated up and cooled down during each thermal stage [10, 11]. These were superseded by Continuous Flow PCR (CFPCR) devices, introduced first by Kopp et al [12], based on single phase flow in a serpentine fluidic channel of rectangular cross-section with three temperature stages in a glass substrate supported by three independent copper block heaters, see Figure 1. Several studies show that, when used in a serpentine arrangement, CFPCR offers reduced reagent consumption and rapid heat transfer, enabling PCR processing times to be reduced dramatically compared to well-based systems. Due to their potential to provide an isolated environment with lower thermal mass than single-phase systems, there are now intensive efforts to create droplet-based PCR systems [6, 10]. However, currently most practical systems use CFPCR based on single-phase flow and these are the focus of the present study. Previous studies of these have shown that the most influential parameters include the substrate's thermal conductivity and the system's thermal resistance, and that fluidic channel sizes and spacing, carrier heat capacity and flow rate and, crucially, the heating arrangement chosen are also all very influential [13].

Controlling the residence times in the denaturation, annealing and extension zones is crucial since insufficient dwell times in each thermal state can seriously degrade DNA amplification efficiency [14]. Residence times in each zone can be optimised by controlling flow rate and channel geometry [15]. Cao et al. [16] explored the role of absolute and relative residence times on DNA amplification efficiency using a combined experimental and numerical approach. The latter employed a Lagrangian modelling approach to predict the temperature

histories of individual DNA molecules flowing through CFPCR devices. Their methodology enabled design times for CFPCR devices to be reduced significantly. A number of other studies have shown that it is also important to control the interference and transition times between the thermal zones, which may require the use of active heating and cooling between the zones, since ordering and interactions between the PCR thermal zones affects PCR yield significantly. These considerations complicate the drive towards CFPCR device miniaturisation, to develop portable devices for diagnostic and testing purposes, since minimising thermal interference between neighbouring serpentine channels tends to lead to wider fluidic devices [14].

The geometry of the serpentine channels is very important and a number of studies have attempted to improve PCR yield by providing a more uniform thermo-flow environment within the PCR zones. Hashimoto et al. [17], for example, used spiral microchannels to reduce reaction times, while other studies have explored the benefits of employing radial [18], spiral [19] and straight channels [20, 21]. Duryodhan et al [22] showed how diverging fluidic channels can create more uniform wall temperatures as a first step to improving the overall temperature uniformity of fluid flowing within the PCR zones. Improved flow uniformity was also achieved through use of electro-kinetic flow to create a plug-like velocity profile to reduce sample dispersion and increase flow-rate control within PCR channels [23].

Selecting appropriate thermal properties which are biologically compatible with the PCR liquid [24], is also very important for CFPCR device optimisation [25], and the goal of minimising the heating power required [26]. Tsuda et al. [27] demonstrated the ability of 3D printing to produce bespoke fluidic reactors with complete control of the 3D fluidic network, a finding which motivated a recent exploration of the potential of using 3D printed serpentine fluidic channels for CFPCR [9]. The flexibility of 3D printing allowed them to explore a number of alternative heating arrangements with heaters located under each of the three temperature zones. They noted that the low thermal conductivity of the 3D printable materials is an important factor limiting their application in CFPCR devices that require rapid heating and cooling.

The above brief review of PCR systems show that their effective design presents a complex multi-objective optimisation problem with several competing objectives, constraints and design variables. Key objectives include the minimisation of total processing time and heating power requirements, and the maximisation of temperature uniformity and DNA amplification efficiency, [28]. There are also important structural constraints on the pressure drop that can be supported by a PCR chip, while the drive towards device miniaturisation constrains the spacing between fluidic channels. These are all influenced by design variables such as flow speeds, fluid and chip thermal properties, the heating arrangements used, fluidic channel and chip dimensions, their channel shape and the distances between the thermal zones, the latter determining the thermal 'cross-talk' between the zones.

Design optimisation based on physics-based simulations is used routinely in the aerospace and automotive industries to solve complex design problems, and several recent advances, that have reduced significantly the time needed to optimise complex flows using CFD, have led to growth in several other applications areas too [29]. The time needed for complex flow simulations, for example, can be reduced significantly by exploiting multi-scale wavelet

methods, which provide efficient surrogates for transferring dynamic, microscale interactions into macroscopic flow simulations, [30], or by using multi-fidelity modelling which enables most of the computational work to be done on cheaper, lower fidelity models, [31]. In addition, advances in design space exploration methods are making large-scale optimisation feasible within practical timescales. R.T. Haftka et al. [32] noted that adjoint methods can now be used to solve large design problems, where the number of design variables is in the 1000s, whereas for problems with $< 100$ design variables (such as the design of PCR systems), gradient-free surrogate-assisted optimisation methods are very effective. Examples of the latter include Moving Least Squares, which is effective at minimising the deleterious effects of numerical noise, [33]. Gaussian Process Emulators also provide very effective statistical surrogates, [34], which can determine confidence intervals around predictions and deal effectively with mixed continuous/categorical design variables, [35]. Supervised Machine Learning (ML) methods also provide powerful surrogate modelling methods with Neural Networks (NNs) and Support Vector Machines (SVMs) having been applied successfully to a range of complex flow systems, [36]. After the surrogate models have been calibrated successfully, they can be implemented within an appropriate multi-objective optimisation algorithm, [37].

The present study proposes a novel Computational Fluid Dynamics (CFD)-enabled optimisation methodology which enables the trade-offs between competing objectives of temperature uniformity, pressure drop and heating power consumption to be explored. This allows designers to maximise the proportion of PCR liquid that experiences the target temperature range for the required time period in each zone, to preserve the structural integrity of the CFPCR chip or to minimise the time taken or overall power consumption (heating and hydraulic) throughout thermal cycling.

The paper is organised as follows. Section 2 describes the numerical methods and the specification of the conjugate heat transfer problem. Section 3 presents the validation of the numerical model and a series of numerical results which demonstrate the dependence of the thermal flow systems on key parameters. Section 4 presents a multi-objective optimisation formulation for PCR flows and a series of CFD and optimisation results which demonstrate the potential to manipulate designs to achieve the competing objectives. Finally, conclusions are drawn in Section 5.

## 2. Numerical Methods

The problem of the microfluidic channel and heating arrangements, together with modelling and numerical methods are described in this section.

### *2.1. Problem Description and Configuration*

The serpentine microfluidic channel, shown in Figure 1, passing through denaturation ($95°C$), annealing ($56°C$) and extension ($72°C$) zones is used as a prototypical CFPCR thermal flow problem. This is based on those considered previously by [14, 17, 38] but with a glass, rather than a PDMS, substrate material to increase thermal conductivity and temperature uniformity. In addition, the cover material ($H_p$ ) used here is PMMA, which can

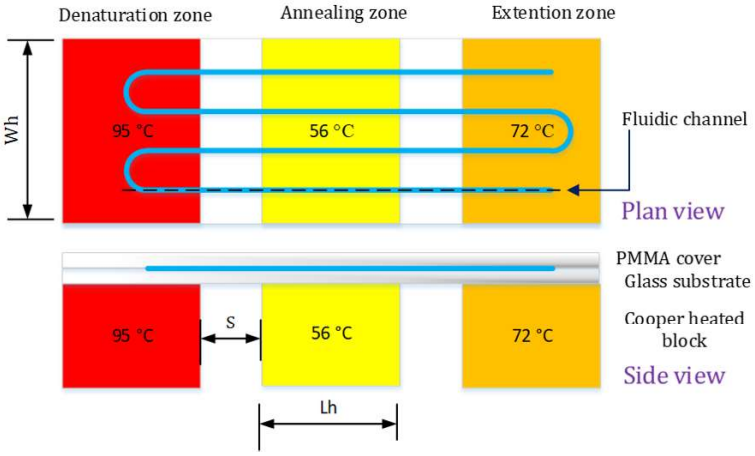


Figure 1: Serpentine PCR systems.

provide good thermal insulation as well as the practical advantages of good optical access and a low cost. A schematic diagram of the microfluidic channel geometry is presented in Figure 2 where $W_c$, $H_c$, $W_w$, $H_b$ and $L$ are the microchannel width, height, wall thickness (the space between the channels), the bottom height and the total length respectively.

There are three individual copper blocks with cartridge heaters placed underneath the glass chip with a constant distance between them of $S = 1mm$, the length of the heaters being $9mm$ underneath the denaturation and annealing zones and $40mm$ underneath the extension zone. The height and length of each heater are $H_h = 2mm$ and $L_h$=$9mm$. The length of the denaturation, annealing and extension zones are chosen to achieve the typical residence time ratios of $1 : 1 : 4$ respectively [38].

### *2.2. Conjugate Heat Transfer Model*

A conjugate heat transfer model of the steady, single-phase, laminar flow problem shown in Figure 2 was developed using the following simplifying assumptions employed by previous studies [38–41]. The liquid is water, with temperature-dependent density, thermal conductivity and viscosity, and the effects of radiation and buoyancy are neglected within the computational domain. There is no internal heat generation.

The Reynolds number ($Re$), is given by:

$$Re = \frac{\rho_f V_{ch} D_h}{\mu_f}, \tag{1}$$

where $\rho_f$ and $\mu_f$ are the density and viscosity of the fluid respectively, $V_{ch}$ is the channel inlet velocity and $D_h$ the channel hydraulic diameter defined by:

$$D_h = \frac{2W_c H_c}{W_c + H_c}. \tag{2}$$

For CFPCR flows, $V_{ch} \sim 1mm/s$, $D_h \sim 10^{-4}$ m and a water density of $10^3 kg/m^3$ and dynamic viscosity $10^{-3} Pa \cdot s$, leads to $Re \sim O(10^{-1})$, i.e. laminar flow conditions.

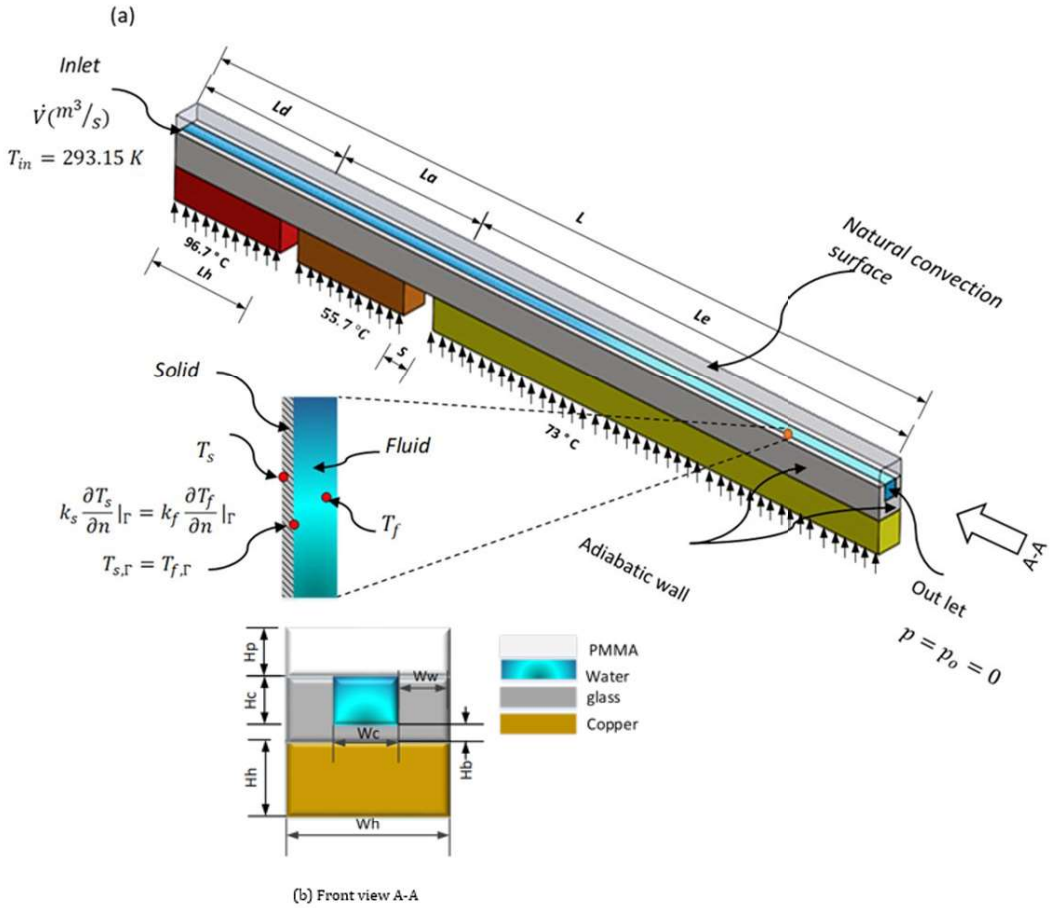


Figure 2: A schematic diagram of the microfluidic channel and heating arrangements in each of the CFPCR zones: a) the thermal boundary conditions applied in each zone and b) the cross-section of the microfluidic channel.

The flow is modelled using the governing continuity and Navier–Stokes equations [42]:

$$\nabla \cdot (\rho_f \mathbf{u}) = 0, \tag{3}$$

and

$$\rho_f(T_f)\left(\mathbf{u}\cdot\nabla\right)\mathbf{u} + \nabla\cdot\left[\mu_f\left(T_f\right)\left(\nabla\mathbf{u} + \nabla^T\mathbf{u}\right) - p\mathbf{I} - \frac{2}{3}\mu_f\left(T_f\right)\nabla\cdot\mathbf{u}\mathbf{I}\right] = 0, \tag{4}$$

where $\mathbf{u}$ and $p$ are respectively the fluid velocity vector and pressure.

The heat transfer is a combination of conduction in the solid domain and convection in the fluid, coupled through conjugate heat transfer boundary conditions at the solid-fluid interface [43]. The energy equation for the convective heat transfer in the fluid is given by

$$\rho_f(T_f)C_{pf}\left(T_f\right)\mathbf{u}\cdot\nabla T_f = \nabla\cdot\left(k_f\nabla T_f\right) + \dot{Q}_{gen}, \tag{5}$$

while the energy equation for conductive heat transfer in the solid is

$$\nabla\cdot\left(k_s\nabla T_s\right) = 0, \tag{6}$$

where $C_{pf}$, $k_f$ and $k_s$ represent the specific heat and thermal conductivities of the fluid and solid respectively. $\dot{Q}_{gen}$ denotes the internal heat generation ($W/m^3$) which is taken to be 0.

The thermo-physical properties of the water ($\rho_f$, $\mu_f$, $C_{pf}$ and $k_f$) depend on the temperature and are given by [44]:

$$\rho_f = 838.466 + 1.4T - 0.003T^2 + 3.72 \times 10^{-7}T^3, \tag{7}$$

$$\begin{aligned}\mu_f =& 1.38 - 0.0212T - 1.36 \times 10^{-4}T^2 - 4.64 \times 10^{-7}T^3 \\ &+ 8.9 \times 10^{-10}T^4 - 9.08^{-13}T^5 + 3.846 \times 10^{-16}T^6,\end{aligned} \tag{8}$$

$$C_{pf} = 12010.147 - 80.407T + 0.3099T^2 - 5.382 \times 10^{-4}T^3 + 3.625 \times 10^{-7}T^4, \tag{9}$$

$$k_f = -0.869 + 0.00895T - 1.584 \times 10^{-4}T^2 - 7.975 \times 10^{-9}T^3, \tag{10}$$

where $T$ is in Kelvin. The thermal conductivity of copper is $k_s = 400W/(m \cdot K)$ and the target temperatures in the denaturation, annealing and extension zones are ($95°C$, $55°C$ and $72°C$) respectively.

*2.2.1. Boundary Conditions*

The computational domain and boundary conditions are shown in Figure 2. At the walls, no-slip velocity boundary conditions $\mathbf{u} = \mathbf{u}_s = 0$ are applied. The inlet velocity $V_{ch}$ is set to achieve a typical Reynolds number of 0.7 and the inlet temperature is fixed at $T_{f,in} = 20°C$, with an ambient pressure condition, $p = p_0$, imposed at the outlet.

The conductive heat transfer in the solid is coupled to the convective heat transfer in the fluid through the following conjugate heat transfer boundary conditions at the solid-liquid interface [43], $\Gamma$: (i) continuity in temperature, $T_{(s,\Gamma)}$=$T_{(f,\Gamma)}$ and (ii) continuity of heat flux given by Fourier's law [45]:

$$-k_s \frac{\partial T_s}{\partial n}|_\Gamma = k_f \frac{\partial T_f}{\partial n}|_\Gamma \tag{11}$$

The upper surface of the domain includes the effect of natural convection via a heat transfer coefficient of $15W/\left(m^2 \cdot K\right)$ [38, 46]. All the outer surface boundary conditions are considered to be adiabatic except at the bottom of the copper heaters where temperatures are set to $96.7°C$, $73°C$ and $55.7°C$ respectively for the denaturation, extension and annealing zones.

The governing equations are solved subject to the boundary conditions using COMSOL Multiphysics 5.4.

### 2.3. Performance Metrics

Three performance metrics are calculated for each flow. The temperature uniformity in the zones is calculated by quantifying deviations from the target temperature, $T_{target}$, via

$$T_{dev} = \sqrt{\frac{\iiint \left(T_{f_{i,j,k}} - T_{target}\right)^2 dV}{\iiint dV}}. \tag{12}$$

The hydraulic performance is measured by calculating the pressure difference along the channel

$$\Delta p = p_{in} - p_{out}. \tag{13}$$

Heating power, $Q$, in each zone $Q_d$, $Q_e$ and $Q_a$ was obtained at the bottom of the heater surfaces using $\mathbf{n} \cdot (k\nabla T) = q/A_h$ where $\mathbf{n}$ denotes the outward normal vector of the domain and $A_h$ is the surface area of the heater. The total heating power is calculated by:

$$Q_t = Q_d + Q_a + Q_e, \tag{14}$$

where $Q_t$, $Q_d$, $Q_a$ and $Q_e$ represent the total heat power in watts ($W$), heat transfer to denaturation zone, and heat extracted from annealing zone and heat transfer to the extension zone respectively.

## 3. Numerical Results

### 3.1. Numerical Validation

The effect of grid density is examined by obtaining numerical solutions on a series of structured Finite Element grids of increasing refinement, on a desktop PC with Microsoft Windows 10 and 32GB physical RAM. Table 1 shows the number of degrees of freedom (DOF), physical memory (PM), Virtual Memory (VM), execution time and calculated $T_{dev}$ and $\Delta p$ for each grid. There is only a small change $< 0.2\%$ in the obtained results if the number of mesh elements is increased above 877552. Accordingly, numerical results presented below have been obtained on the mesh with 877552 elements as an appropriate compromise between computational expense and accuracy.

| NO. of elements | DOF ($\times 10^5$) | PM (GB) | VM (GB) | Time | $\Delta p(Pa)$ | $T_{dev}$ |
|---|---|---|---|---|---|---|
| 93024 | 2.52 | 2.71 | 3.28 | 119 | 51.31 | 27.98 |
| 216096 | 5.1679 | 3.17 | 3.92 | 303 | 51.00 | 27.81 |
| 380480 | 8.3090 | 3.89 | 4.67 | 553 | 50.64 | 27.70 |
| 448686 | 14.485 | 4.47 | 5.26 | 677 | 50.58 | 27.58 |
| 877552 | 17.763 | 6.56 | 7.42 | 1839 | 50.48 | 27.57 |
| 1026602 | 20.373 | 8.23 | 9.52 | 3849 | 50.45 | 27.50 |
| 1171632 | 23.329 | 7.93 | 8.92 | 4050 | 50.43 | 27.52 |

Table 1: Effect of grid density for the case of $Re = 0.7$, $T_f = 20°C$, $H_c = 150\mu m$, $W_c = 500\mu m$, $W_w = 150\mu m$ and $H_b = 850\mu m$.

The numerical model is first compared with the experimental results of [22] for thermal flow in diverging channels. Figure 3 shows that the agreement between the experimental and numerical results is generally very good. The next comparison is with the numerical results of [38] where $H_c = 150\mu m$, $W_c = 50\mu m$, $S = 1mm$, $V_{ch} = 6mm/s$ and $T_{f,in} = 72°C$. Once again the numerical predictions of the temperature profile along the three temperature zones, shown in Figure 4, are in very good agreement with the published results.

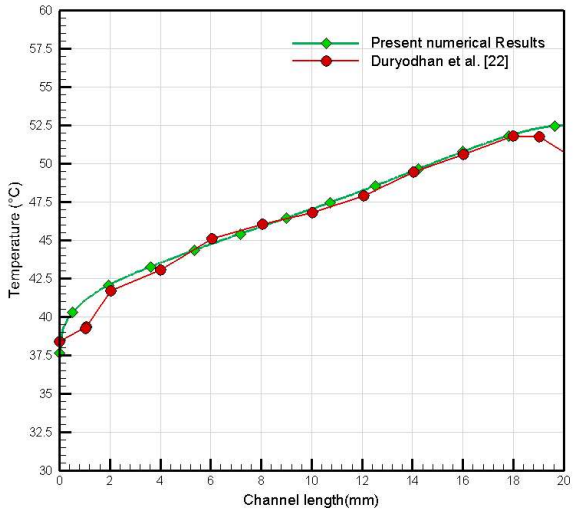


Figure 3: Comparison of surface temperature variation along flow direction in a diverging microchannel at $q = 4W$.

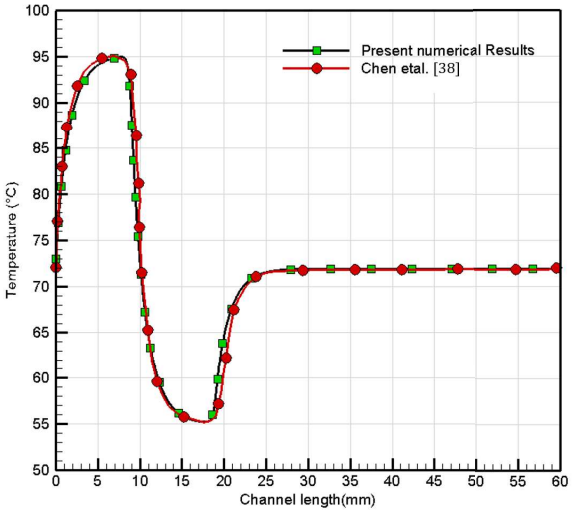


Figure 4: Comparison of fluid average temperature profile along the centreline of CFPCR zones.

### *3.2. One-dimensional (1-D) thermal modelling*

Several previous studies of heat transfer in micro-channel structures have employed simplified analyses successfully. For small channels with $D_h \sim 50\mu m$, convective heat transfer can often be neglected [23] and for flows which are fully developed thermally, 1-D models may also be useful. The thermal entrance length for laminar flow can be estimated by [47]

$$L_{th} = 0.05 RePr D_h \tag{15}$$

where $Pr$ is the Prandtl number given by

$$Pr = \frac{C_p \mu}{k}. \tag{16}$$

For the cases considered here $L_{th} \sim 20\mu$m so the thermal entrance length can be neglected. By applying the energy balance approach described in [44, 48] the average flow temperature, $T_{f,avg}$, for the constant wall temperature, $T_w$, is given by

$$T_{f,avg}(x) = T_w - (T_w - T_{in}) \times \exp(-h^{'}.P.x/\dot{m}C_{pf}) \tag{17}$$

where $x$ is the distance along the channel, $T_{in}$ is the fluid inlet temperature, $\dot{m}$ is the mass flow rate, $h^{'}$ is a heat transfer coefficient, $P$ is the perimeter of the microchannel and $C_{pf}$ is the fluid heat capacity. The Nusselt number for fully developed laminar flow inside a channel heated at constant wall temperature can be calculated based on correlation proposed by Shah [49]

$$Nu = 7.541(1 - 2.61\epsilon + 4.97\epsilon^2 - 5.119\epsilon^3 + 2.702\epsilon^4 - 0.548\epsilon^5) \tag{18}$$

where $\epsilon = W_c/H_c$. Two different values of $h^{'}$ are used in the solution (17). Model 1 obtains $h^{'} = h$ from:

$$Nu = hD_h/k \tag{19}$$

while the model 2 uses this value of $h$ within an effective heat transfer coefficient $h^{'}$ proposed by [50, 51] :

$$h^{'} = [1/h + H_b/k_s]^{-1} \tag{20}$$

that accounts for the effects of substrate thickness. Predictions of the 1-D models (17) are compared with those of the 3-D conjugate heat transfer model in Figure 5, for the thermal conditions specified in the denaturation zone. Figure 5(a) shows that for the case with $V_{ch}$=4mm/s and zero substrate thickness, $H_b = 0\mu m$, the agreement is excellent. However for cases with larger values of $H_b$, the discrepancy between the models is more significant due to the thermal resistance of the substrate, although the effective heat transfer coefficient (20) does improve predictions for the thicker substrate. More generally, it is found that the 1-D model works well provided the conductive thermal resistance, defined by $R_{th} = H_b/k_s$, is small. This cannot be neglected for cases considered below, with larger substrate thicknesses, and for which full 3-D simulations are required.

### *3.3. Effect of substrate material*

The effect of the substrate material on the temperature profile is considered next, for flow in a channel with dimensions: $H_c = 150\mu m$, $W_c = 500\mu m$, $H_b = 850\mu m$, $W_w = 50\mu m$, $H_h = 2000\mu m$, $H_{PMMA} = 1500\mu m$ and $S = 1mm$. Figure 6 shows the effect of the material on the fluid temperature profile at the low inlet flow velocity $V_{ch} = 0.1mm/s$. The fluid temperatures in these cases are reasonably uniform for all materials, with the fluid temperature for glass and silicone chips being closest to the target temperatures in the zones while that for the polyimide chip is furthest from the target profile. The size of the deviations from the target temperature profiles generally decreases as the thermal conductivity of the chip material increases due to the smaller thermal resistance between the heated substrate and the flowing liquid. As noted by Chen et al. [14], this can however lead to greater thermal interference between zones.

Figure 7 shows the effect of increasing the inlet velocity to $V_{ch} = 1mm/s$. This leads to greater discrepancies from the target temperatures in each zone, since convective heat transfer becomes more significant at the higher speed. Once again, the deviations from the target temperature profile decrease as thermal conductivity increases. Figure 8 summarises the effect of material and inlet flow velocity on the deviations from the target temperatures, and quantifies the monotonic increases in $T_{dev}$ as $V_{ch}$ increases and thermal conductivity decreases, due to the increased convection and thermal resistance respectively.

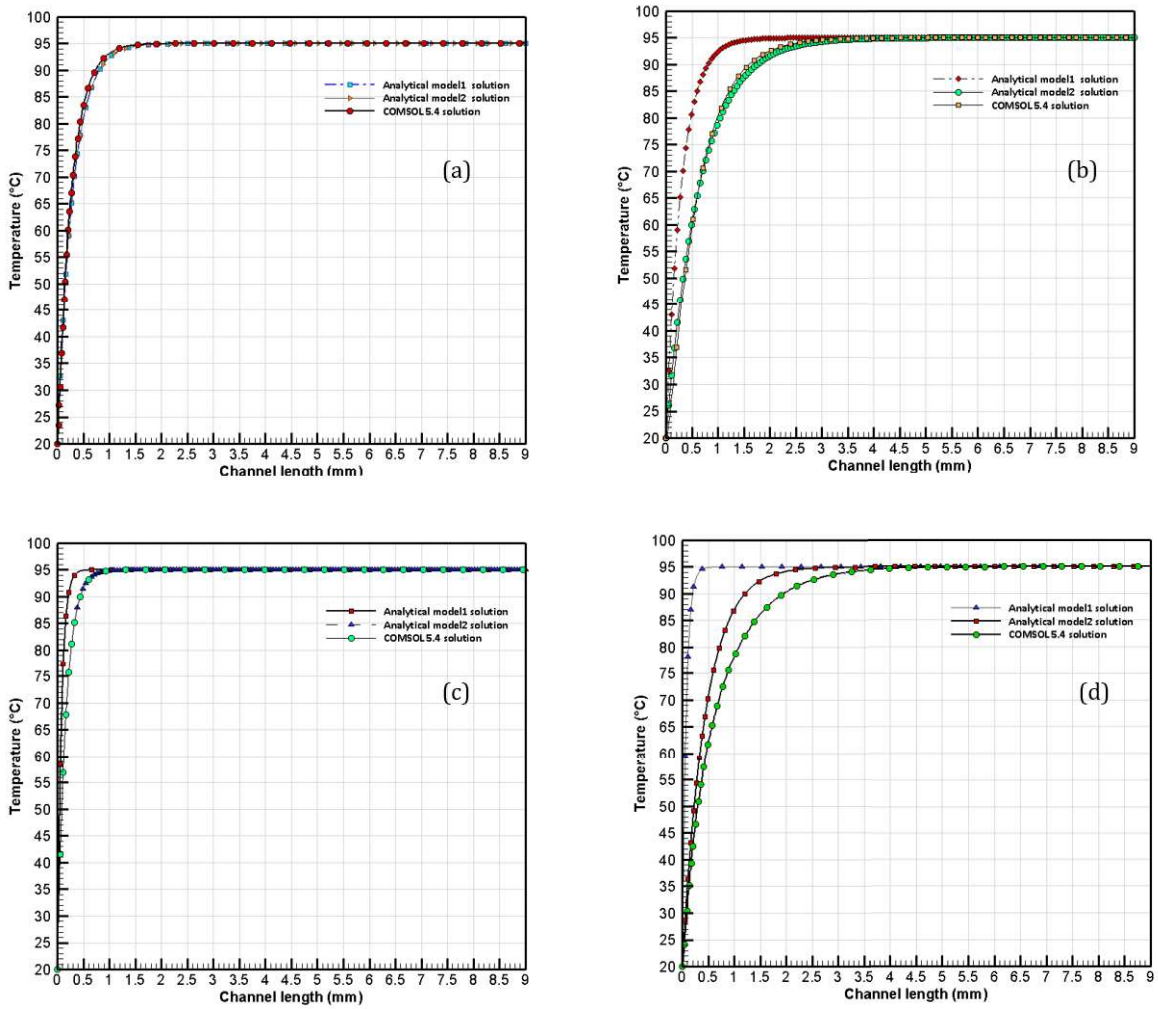


Figure 5: Comparison of 1-D and CFD predictions of centreline temperature in the CFPCR denaturation zone with (a) $V_{ch}$=4mm/s, $H_b$=0 $\mu m$; (b) $V_{ch}$=4mm/s, $H_b$=200$\mu m$; (c) $V_{ch}$=1mm/s, $H_b$=200$\mu m$; (d) $V_{ch}$=1mm/s, $H_b$=850$\mu m$

It is instructive to calculate two dimensionless parameters for the present problems. The first, the Peclet number, quantifies the relative importance of convection compared to conduction in the liquid and is defined by Lin et al. [52]:

$$P_e = V_{ch}.D_h/\alpha \tag{21}$$

where $\alpha$ is the thermal diffusivity of the liquid. The second assesses the importance of axial conduction compared to convection in micro-scale systems and is defined by Maranzana et al. [53]:

$$M = q_{cond}/q_{conv} = (k_s.H_b)/(\rho_f.C_{pf}.H_c.V_{ch}) \tag{22}$$

Values are given in Table 7 for examples of the cases considered here.

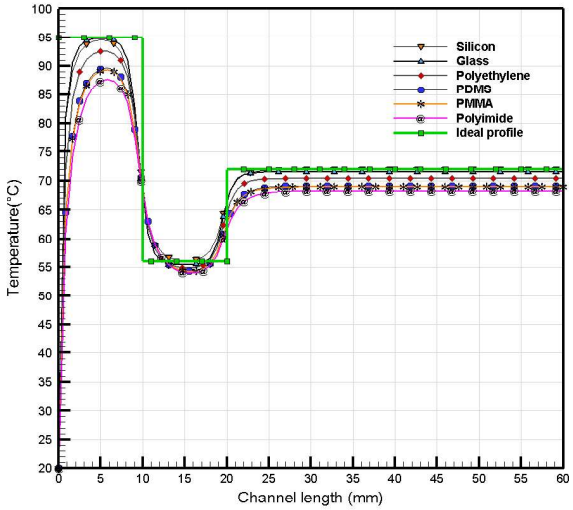


Figure 6: Temperature profile along the centerline of CFPCR zones at $V_{ch} = 0.1mm/s$.

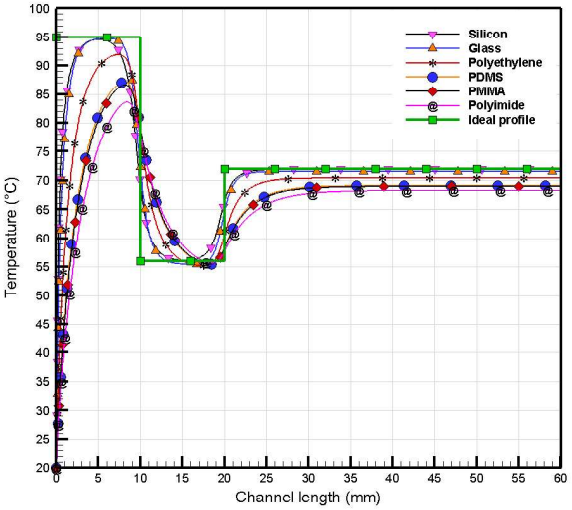


Figure 7: Temperature profile along the centerline of CFPCR zones at $V_{ch} = 1mm/s$.

| **Material** | $T_{dev}$ $(^\circ C)$ | | | $Pe$ | | | $M$ | | |
|---|---|---|---|---|---|---|---|---|---|
| | $V_{ch1}$ | $V_{ch2}$ | $V_{ch3}$ | $V_{ch1}$ | $V_{ch2}$ | $V_{ch3}$ | $V_{ch1}$ | $V_{ch2}$ | $V_{ch3}$ |
| Polyimide | 44.522 | 73.888 | 94.613 | 1.442 | 8.850 | 14.978 | 0.0034 | $5.81\times10^{-4}$ | $3.49\times10^{-4}$ |
| PMMA | 40.336 | 63.988 | 84.747 | 1.439 | 8.794 | 14.858 | 0.0044 | $7.35\times10^{-4}$ | $4.41\times10^{-4}$ |
| PDMS | 39.448 | 62.881 | 82.573 | 1.439 | 8.783 | 14.834 | 0.00463 | $7.74\times10^{-4}$ | $5.36\times10^{-4}$ |
| Polyethylene | 29.665 | 57.753 | 61.778 | 1.434 | 8.679 | 14.583 | 0.0088 | 0.00148 | $8.82\times10^{-4}$ |
| Glass | 19.366 | 38.309 | 47.790 | 1.430 | 8.597 | 14.359 | 0.0324 | 0.0054 | 0.0032 |
| Silicon | 18.152 | 20.799 | 22.922 | 1.428 | 8.575 | 14.295 | 3.0129 | 0.502 | 0.301 |

Table 2: The effect of chip material and inlet velocity on $T_{dev}$, $Pe$ and $M$ for $V_{ch1} = 1mm/s$, $V_{ch2} = 6mm/s$, $V_{ch3} = 10mm/s$, for $H_b = 850\mu m$.

Since $Pe > 1$ convection is influential in all cases and temperature variations along the channel result from the competition between convection, which acts to increase them, and conduction, which acts to reduce them. Lower axial conduction for the particular case of PMMA at $V_{ch}$=1mm/s may explain why its $T_{dev} = 40.336$ is greater than $T_{dev} = 38.309$ for glass at the much higher velocity $V_{ch}$=6mm/s.

In view of its good thermal and optical properties, all results below use glass as the substrate material. Figure 9 and Table 2 show how the temperature variation $T_{dev}$ in glass chips is affected by channel inlet velocity $V_{ch}$ and demonstrates clearly how the temperature profile throughout the three PCR zones is very different from the target profile at the higher speeds.

The effect on heating power is considered next. Figure 10 and Table 3 show that the heating power consumption increases as the velocity increases and that the comparatively

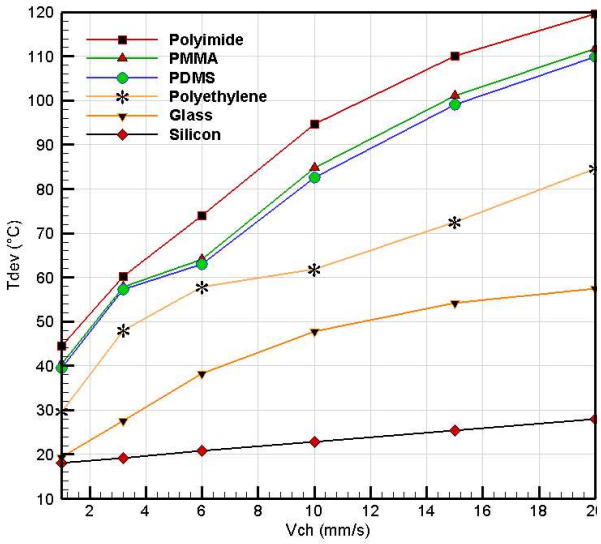


Figure 8: The effect of material type on the PCR performance responses in terms of $T_{dev}$ at different inlet velocity $V_{ch} = (1 - 20)mm/s$.

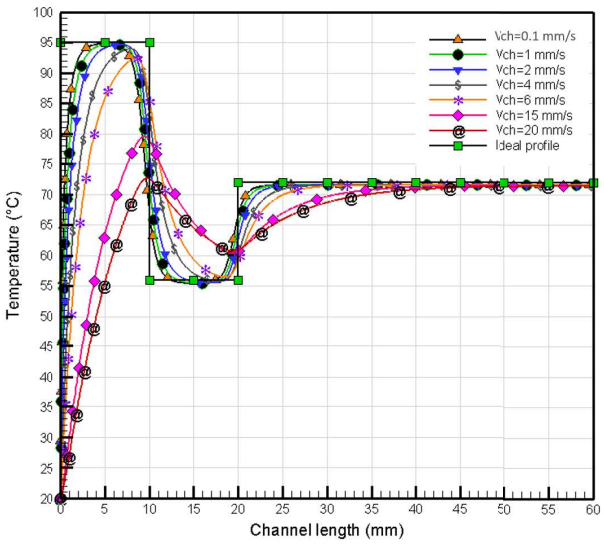


Figure 9: Temperature profile along the centerline of CFPCR zones at different velocities using a glass substrate.

| **Material** | $Q_t(W)$ | | | | |
|---|---|---|---|---|---|
| | $k_s(W/m.K)$ | $V_{ch1}$ | $V_{ch2}$ | $V_{ch3}$ | $V_{ch4}$ |
| Polyimide | 0.15 | 0.054 | 0.105 | 0.146 | 0.183 |
| PMMA | 0.19 | 0.058 | 0.109 | 0.157 | 0.203 |
| PDMS | 0.2 | 0.059 | 0.111 | 0.160 | 0.207 |
| Polyethylene | 0.38 | 0.071 | 0.164 | 0.195 | 0.246 |
| Glass | 1.4 | 0.122 | 0.283 | 0.393 | 0.475 |
| Silicon | 130 | 5.293 | 5.384 | 5.476 | 5.607 |

Table 3: The effect of chip material on heating power required for $V_{ch1} = 1mm/s$, $V_{ch2} = 6mm/s$, $V_{ch3} = 10mm/s$, $V_{ch4} = 15mm/s$.

high thermal conductivity of silicon leads to at least an order of magnitude larger heating power requirement.

The results show that $T_{dev}$ is influenced by the competition between convection and axial conduction that results from the material type, flow rate and channel size. In practice, there are other competing objectives which need to be considered, such as the need to minimise the pressure drop and heating power consumption. The next section extends the analysis to formulate and solve multi-objective optimisation problems relevant to PCR systems.

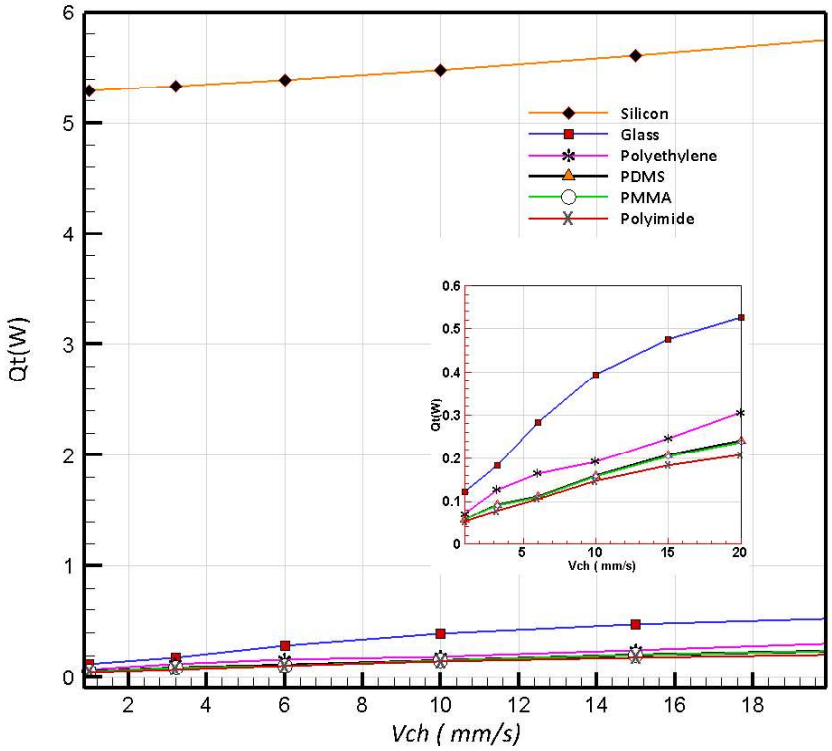


Figure 10: The effect of material type and inlet velocity $V_{ch}$ on the heating power requirement.

## 4. Optimisation

As surrogate-enabled, multi-objective optimisation methodology [32] is developed to explore the compromises that can be struck between temperature uniformity throughout the three zones and the pressure drop and heating power required. Its key steps are:

1. Formulate the optimisation problem: specify the objective functions and constraints.
2. Design space parameterisation: specify the design variables and design space.
3. Design of experiments (DoE): generate a relatively small number of well-scattered design points throughout the design space.
4. CFD solutions: obtain CFD solutions of the conjugate heat transfer problem at each of the DoE points and extract values of the objective functions from them.
5. Surrogate modelling: build and validate accurate surrogate models for each objective function throughout the design space using an appropriate surrogate modelling method.
6. Multi-objective optimisation: embed the surrogate models within an appropriate multi-objective optimisation algorithm and generate Pareto surfaces showing optimal compromises between each objective function and validate their accuracy against the CFD solutions at selected Pareto points.

### 4.1. Problem Formulation

The prototype three-zone PCR system is optimised according to the competing objectives of minimising each of the temperature deviation, $T_{dev}$, pressure drop, $\Delta p$, and heating power, $Q_t$, defined in section 2.3. The influence of the four design variables $W_c$, $H_c$, $H_b$ and $W_w$ is explored at a constant Reynolds number $Re = 0.7$, and with constant $T_{f,in} = 20°C$, $S = 1mm$, $H_h = 2mm$, $H_p = 1.5mm$ and $L = 60mm$. Temperatures at the bottom of the copper heaters over the denaturation, extension and annealing zones are set at $96.7°C$, $73°C$ and $55.76°C$ respectively. The multi-objective optimisation problem considered here is the minimisation of each of $\{T_{dev}, \Delta p, Q_t\}$ within the design space:

$$150\mu m \leq W_c \leq 500\mu m, 50\mu m \leq H_c \leq 150\mu m, 400\mu m \leq H_b \leq 800\mu m, 70\mu m \leq W_w \leq 800\mu m.$$

### 4.2. Effect of channel size

Table 4 shows typical results of varying the channel dimensions, $W_c$ and $H_c$, on the pressure drop $\Delta p$ and temperature deviation $T_{dev}$. Pressure drop $\Delta p$ is effectively independent of $H_b$ and $W_w$ and depends only on the $W_c$ and $H_c$ through a strong dependence on channel cross-sectional area, $W_c \times H_c$. In contrast, $T_{dev}$ also depends on $H_b$ through its influence on the substrate thermal resistance. As $H_b$ increases, conduction into the liquid decreases leading to larger temperature variations.

| Case no. | $W_c$(mm) | $H_c$ (mm) | $H_b$(mm) | $\Delta p(Pa)$ | $T_{dev}(K)$ |
|---|---|---|---|---|---|
| 1 | 0.5 | 0.15 | 0.8 | 50.27 | 26.04 |
| 2 | 0.5 | 0.05 | 0.8 | 993.62 | 22.52 |
| 3 | 0.15 | 0.15 | 0.8 | 147.59 | 25.74 |
| 4 | 0.15 | 0.05 | 0.8 | 1416.10 | 20.44 |
| 5 | 0.5 | 0.15 | 0.4 | 49.92 | 19.71 |
| 6 | 0.5 | 0.05 | 0.4 | 986.33 | 16.66 |
| 7 | 0.15 | 0.15 | 0.4 | 146.67 | 19.34 |
| 8 | 0.15 | 0.05 | 0.4 | 1413.30 | 15.30 |

Table 4: Effect of channel size on $T_{dev}$ and $\Delta p$ for the case of $Re = 0.7$, $T_f = 20°C$, $W_w = 0.07$mm.

### 4.3. Design of experiments (DOE) and CFD solutions

After choosing the range of the design variables, design of experiments (DOE) points were generated and distributed within design space using an Optimal Latin Hypercube Sampling technique [54]. CFD simulations were then run at these design points to generate the $\mathbf{y} = (T_{dev}, \Delta p, Q_t)$ data set for use within the surrogate models.

### 4.4. Surrogate Modelling

Two surrogate modelling approaches are used. The first is based on cubic Radial Basis Functions (RBFs) where the surrogate model $y_k$ ($k^{th}$ component of $\mathbf{y}$ with $k = 1, 2, 3$) for the output variable $\mathbf{y}$ at a design point $\mathbf{x} = (W_c, H_c, H_b, W_w)$ is given by

$$y_k(\mathbf{x}) = \sum_{i=1}^{N} \lambda_i \phi\left(\|\mathbf{x} - \mathbf{x}_i\|\right), \quad \phi\left(\|\mathbf{x} - \mathbf{x}_i\|\right) = \beta\|\mathbf{x} - \mathbf{x}_i\|^3, \tag{23}$$

with $\mathbf{x}_i$ being the $i^{th}$ DoE point ($1 \leq i \leq N$), taken from $N = 560$ CFD simulations. $\|\cdot\|$ denotes the $l^2$ norm, $\lambda_i$ are RBF parameters. $\beta$ is a calibration parameter for the cubic RBF function. For each surrogate model $\beta$ is determined using a relatively simple Leave-One-Out (LOO) calibration, where each sample point is left out of the RBF function and then used to predict the value at the omitted DoE point. The Root Mean Square Error (RMSE) of the discrepancies between the predicted and actual DoE points is then minimised with respect to the $\beta$ parameter over a suitable interval [33].

The second approach uses fully connected Neural Networks (NNs) available within Tensor Flow, using $N_{train}$=176 of these randomly selected for the training data set and the remaining $N_{tests}$=50 used as the test data set. A Stochastic Gradient Descent (SGD) method is used to minimise the cost function:

$$cost = \sum_{i=1}^{N_{train}} \|\mathbf{y}_i^{predict} - \bar{\mathbf{y}}_i^{train}\|/N_{train}. \tag{24}$$

The calculations are terminated after $5 \times 10^4$ iterations to avoid over-fitting when the error

$$err = \sum_{i=1}^{N_{train}} \|\mathbf{y}_i^{predict} - \bar{\mathbf{y}}_i^{test}\|/N_{test} \tag{25}$$

does not decrease as shown in Figure 11.

In (24) and (25), $\bar{\mathbf{y}}$ is the normalised data set given by

$$\bar{y}_k = \frac{y_k - y_{k,min}}{y_{k,max} - y_{k,min}}, \quad (k = 1, 2, 3) \tag{26}$$

with $y_k$ being the $k^{th}$ component of $\mathbf{y}$, and $y_{k,min}$ ($y_{k,max}$) being the minimum (maximum) of all the $N$ data points for the $k^{th}$ component.

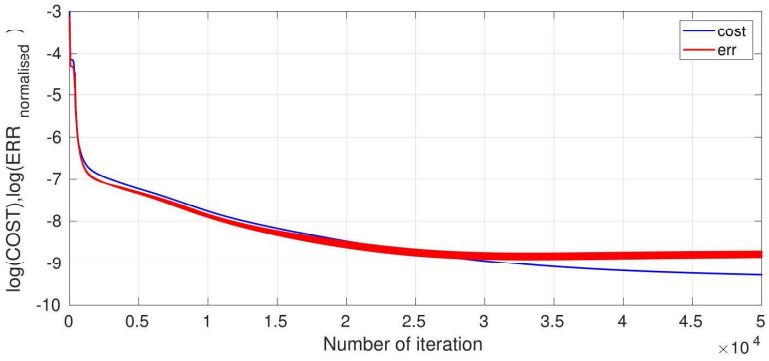


Figure 11: Convergence of the cost function evaluated on the training data and error measured on the test data set.

The training procedure random process is performed 10 times for the same NN before the effect of using different topologies is explored. The three best NNs that can reduce the error in the testing dataset to around 0.3% are shown in Figure 12.

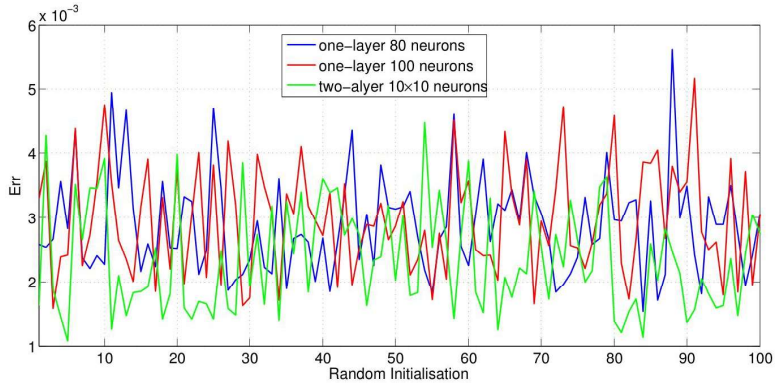


Figure 12: Final error of running the same NN 100 times, which is initialized randomly.

A reliable method of determining the best NN is to let them predict another unseen data set. Therefore these three NNs are tested on 50 additional CFD data points, and the relative error is shown in Table 5. From these we can conclude that the one-layer NN with 100 neurons is the most accurate, and will be used in all NN results presented below.

| One-layer NN with 80 neurons | one-layer NN with 100 neurons | Two-layer NN with $10 \times 10$ neurons |
|---|---|---|
| $3.5773 \times 10^{-3}$ | $2.0128 \times 10^{-3}$ | $2.4820 \times 10^{-3}$ |

Table 5: Error testing on 50 additional data points.

### *4.5. Single-Objective optimisation*

Optimising each of the objectives in isolation is relatively straightforward and valuable insight can be obtained from examining the surrogate models of each individual objective. Figure 13 shows examples of surrogate model surfaces for $T_{dev}$, which indicate that minimising $T_{dev}$ requires the smallest $W_c$, $H_c$ and $H_b$ values. Similar insights can be gained by examining the surrogate models for the other objectives. The global minima for each individual objective are shown in Table 6: for example, the first row shows the design point corresponding to the global minimum for the objective $T_{dev}$, together with the other two objectives at this point. Note that the minimum value of $T_{dev}$ corresponds to comparatively large values of $\Delta p$ and $Q_t$, whereas the minimum $\Delta p$ corresponds to comparatively large $T_{dev}$ and $Q_t$. This indicates that it is interesting to explore the trade-off between the objective functions through a multi-objective analysis.

### *4.6. Multi-Objective Pareto Analysis*

The RBF and NN methods were used to create Pareto curves of non-dominated solutions for $\Delta p$ vs $T_{dev}$, $\Delta p$ vs $Q_t$ and $T_{dev}$ vs $Q_t$. The RBF method uses the Multi-Objective Genetic Algorithm (MOGA) solver in MATLAB, whereas the NN methods use the SciPy.optimization module in Python based on a simple weighting between the competing

| Objective | Global min. | $W_c$(mm) | $H_c$ (mm) | $H_b$(mm) | $W_w$ (mm) | $T_{dev}(K)$ | $\Delta p(Pa)$ | $Q_t(W)$ |
|---|---|---|---|---|---|---|---|---|
| $T_{dev}(K)$ | 12.864 | 0.150 | 0.050 | 0.400 | 0.727 | - | 1426.464 | 0.192 |
| $\Delta p(Pa)$ | 49.782 | 0.500 | 0.150 | 0.799 | 0.799 | 19.684 | - | 0.381 |
| $Q_t(W)$ | 0.063 | 0.150 | 0.050 | 0.400 | 0.070 | 15.307 | 1413.317 | - |

Table 6: Single objective optimisation.

objectives. The Pareto curves from the RBF and NN meta-modelling are all very similar to each other - the Pareto curves for $\Delta p$ vs $T_{dev}$ are shown in Figure 14 and its accuracy is confirmed by the further validation with the CFD predictions at points P1-P7 shown in Table 7. This provides a basis for finding an appropriate balance between these competing objectives. It shows, for example, that reducing $T_{dev}$ from 14 to 13 would require a four-fold increase of $\Delta p$, from 250 to $1000Pa$, while reducing $\Delta p$ below $100Pa$ comes at the price of a sharp rise in $T_{dev}$.

Figure 15 compares the temperature profile from a design point on the Pareto curve ($H_c = 50\mu m$, $W_c = 152\mu m$, $H_b = 403\mu m$, $W_w = 667\mu m$, $H_h = 2000\mu m$, $H_{PMMA} = 1500\mu m$ and $S = 1mm$) with that from a non-optimised Design of Experiments point ($H_c = 150\mu m$, $W_c = 500\mu m$, $H_b = 800\mu m$, $W_w = 70\mu m$, $H_h = 2000\mu m$, $H_{PMMA} = 1500\mu m$ and $S = 1mm$). It can be seen that the temperature profile from the optimised solution is much closer to the target temperature profile than for the non-optimised one.

Figure 16 shows the other two-dimensional Pareto curves for the competing objectives $\Delta p$ vs $Q_t$ and $T_{dev}$ vs $Q_t$, obtained using the one-layer NN with 100 neurons available in TensorFlow, combined with the SciPy.optimization module. Figure 16(a) shows that $Q_t$ can be reduced significantly without a major pressure drop penalty, but that reducing it below 0.06 does require a significantly larger $\Delta p$. Figure 16(b) shows that there is a reasonably linear, negative correlation between $T_{dev}$ vs $Q_t$ for $T_{dev} > 13$ but that $Q_t$ increases sharply for lower values of $T_{dev}$. Finally, Figure 17(a) extends the Pareto analysis to consider all three competing objectives, $T_{dev}$, $\Delta p$ and $Q_t$ simultaneously. The non-linearities make it difficult to fit all the Pareto points onto a smooth surface, however it is possible to create smooth Pareto surfaces over subsets of the design space, see Figure 17(b). These surfaces provide a scientific basis for achieving an appropriate balance between these three competing objectives, based on practical design requirements.

## 5. Conclusion

This paper proposes the first CFD-enabled optimisation methodology for thermal flow in PCR systems, accounting for temperature uniformity, pressure losses and heating power requirements. Results have shown that temperature variations in the PCR liquid along zones is determined by the competition between convection and conduction in the vertical and axial directions, with the former acting to exacerbate temperature variations and the latter to reduce them. The temperature variations are a nonlinear function of flow rate, channel size, substrate material thermal properties and substrate dimensions. Generally, reducing both the flow rate, which reduces convection, and substrate thermal resistance,

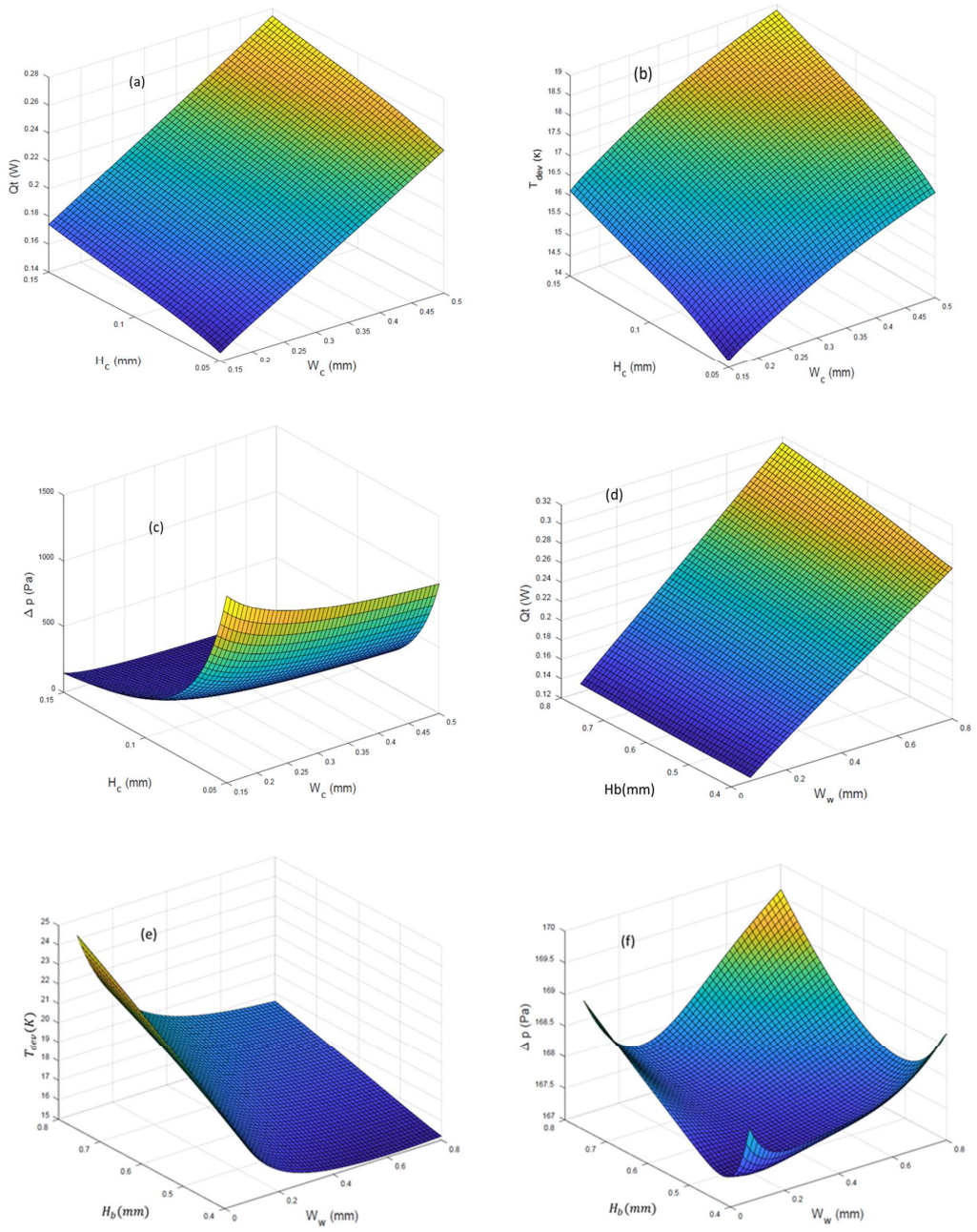


Figure 13: Typical surrogate model surfaces of $T_{dev}$ as a function of (a) $H_c$ vs $W_c$ (with $H_b = 0.6$, $W_w = 0.435$), (b) $H_c$ vs $W_c$ (with $H_b = 0.6$, $W_w = 0.435$, (c) $H_c$ vs $W_c$ (with $H_b = 0.6$, $W_w = 0.435$), (d) $H_b$ vs $W_w$ (with $H_c = 0.1$, $W_c = 0.325$), (e) $H_b$ vs $W_w$ (with $H_c = 0.1$, $W_c = 0.325$), (f) $H_b$ vs $W_w$ (with $H_c = 0.1$, $W_c = 0.325$.)

$R_{th} = H_b/k_s$, which increases conduction into the liquid, decreases temperature deviations along a channel. The values of the Peclet and axial conduction numbers can provide further, valuable insight into the relative importance of convection and conduction and their influence

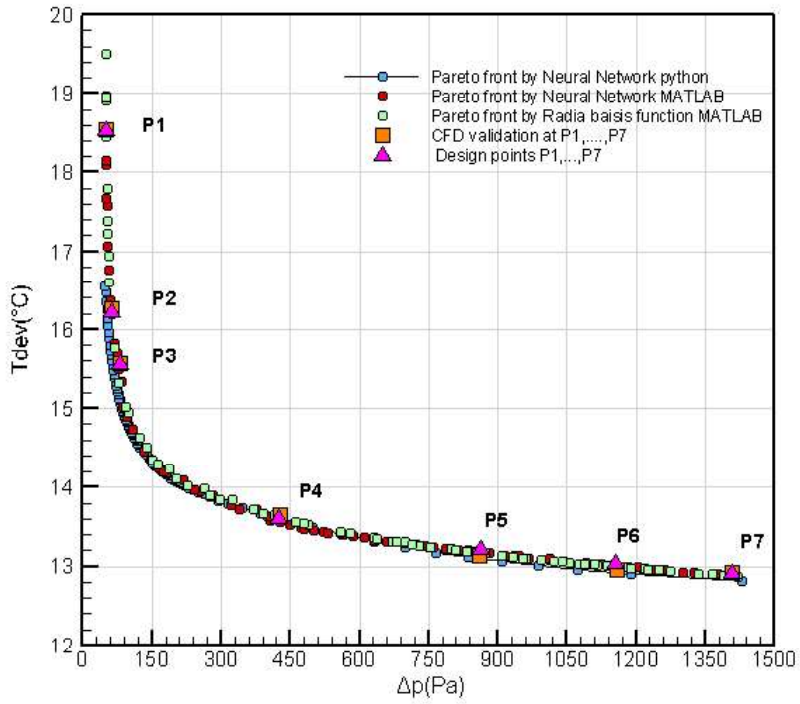


Figure 14: Pareto curves of $\Delta p$ vs $T_{dev}$, obtained using RBF and NN surrogate modelling.

| **points** | Geometrical dimensions(mm) | | | | $\Delta p$ $(pa)$ | | $T_{dev}$ $(K)$ | | $error\%$ | |
|---|---|---|---|---|---|---|---|---|---|---|
| | $H_b$ | $H_c$ | $W_c$ | $W_w$ | $Pareto$ | $CFD$ | $Pareto$ | $CFD$ | $\Delta p$ | $T_{dev}$ |
| P1 | 0.624 | 0.149 | 0.467 | 0.557 | 51.679 | 51.528 | 18.526 | 18.534 | 0.294 | 0.040 |
| P2 | 0.441 | 0.145 | 0.363 | 0.636 | 63.903 | 63.552 | 16.215 | 16.272 | 0.552 | 0.347 |
| P3 | 0.453 | 0.149 | 0.246 | 0.637 | 80.166 | 80.445 | 15.555 | 15.570 | 0.346 | 0.094 |
| P4 | 0.404 | 0.083 | 0.152 | 0.688 | 426.179 | 427.880 | 13.603 | 13.642 | 0.397 | 0.284 |
| P5 | 0.402 | 0.061 | 0.150 | 0.696 | 862.899 | 859.140 | 13.201 | 13.131 | 0.437 | 0.536 |
| P6 | 0.402 | 0.054 | 0.150 | 0.696 | 1155.840 | 1157.20 | 13.030 | 12.965 | 0.117 | 0.508 |
| P7 | 0.402 | 0.050 | 0.150 | 0.717 | 1408.68 | 1407.5 | 12.897 | 12.922 | 0.083 | 0.192 |

Table 7: PCR design performance at seven operating conditions points located on the Pareto front together with CFD validation as shown in Figure .

on temperature uniformity. The dependence of pressure drop and heating power on design variables is much simpler. The former only depends on the channel sizes, $W_c$ and $H_c$, and increases rapidly as channel cross-sectional area $W_c \times H_c$ decreases, whereas heating power requirements depend mainly on the substrate thermal conductivity, with results showing those for silicon being an order of magnitude larger than for the other materials considered.

If obtaining high levels of temperature uniformity is the key consideration then it is

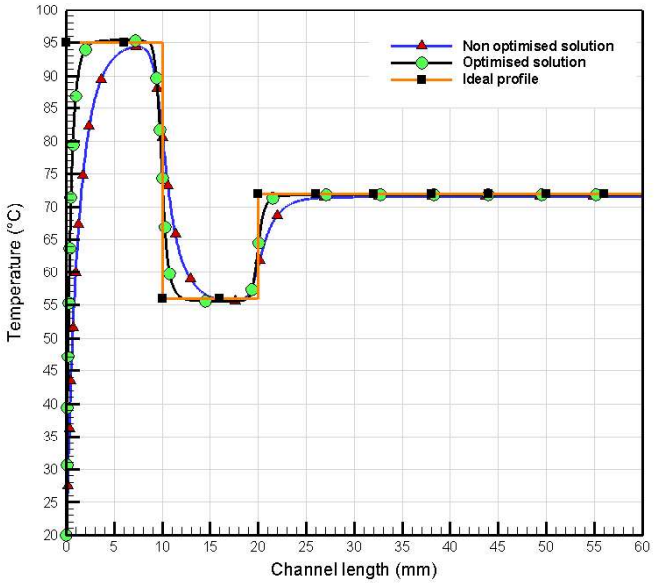


Figure 15: A comparison of temperature profiles in PCR fluidic channel from an optimised and a non-optimised solution.

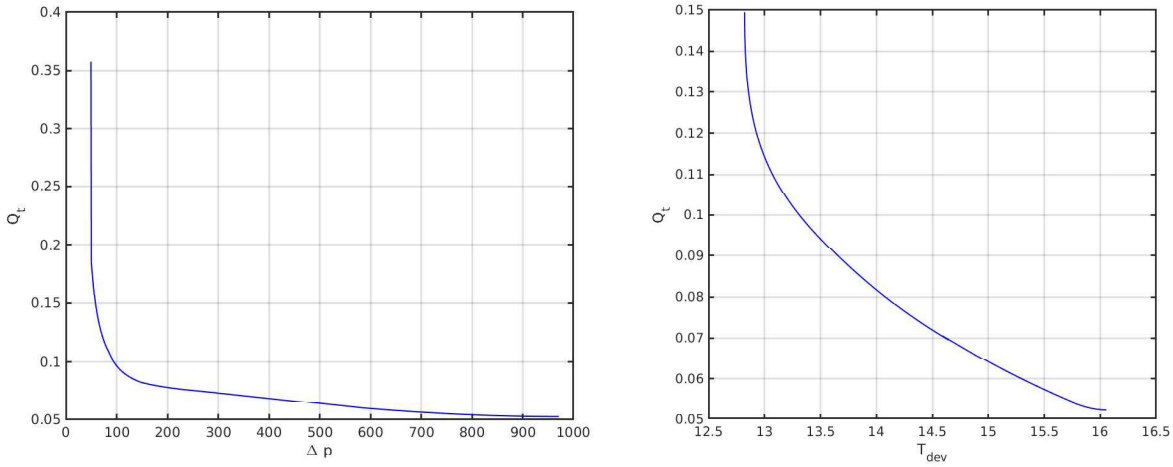


(a) $\Delta p$ vs $Q_t$.

(b) $T_{dev}$ vs $Q_t$.

Figure 16: Pareto curves of the competing objectives.

possible to choose a substrate with high conductivity, small substrate thickness and small channel area. However since there are often important structural constraints on the pressure drop that can be supported by a PCR chip, then it would be necessary to choose a larger channel area to reduce pressure drop. This paper has shown that a multi-objective optimisation methodology can provide the information designers need to make these deci-

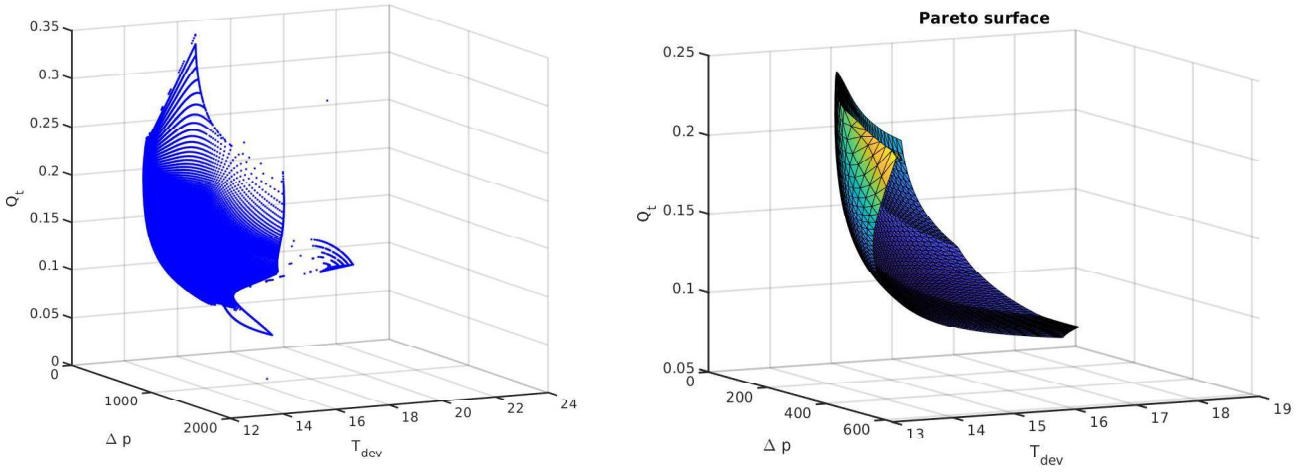


(a) Pareto set as discrete points.

(b) Part of the Pareto set fitted to a smooth surface.

Figure 17: Three dimensional Pareto set.

sions in a scientifically-rigorous manner. Pareto curves from the multi-objective optimisation methodology demonstrate clearly the compromises that can be struck between temperature uniformity, pressure drop and heating power throughout the three zones. For example, these have quantified the price that must be paid in terms of increased pressure drop and heating power in order to get high temperature uniformity in the zones. The proposed optimisation framework is generic and can be extended to account for other practical objectives, such as the DNA amplification achieved throughout the PCR zones.


## Acknowledgements:

The authors are grateful to the Ministry of Oil, Iraq, and British petroleum (BP), Iraq, for sponsoring the work on this project. This work was undertaken on ARC4, part of the High Performance Computing facilities at the University of Leeds, UK.


## References


[1] A. D. Stroock, S. K. Dertinger, A. Ajdari, I. Mezić, H. A. Stone, G. M. Whitesides, Chaotic mixer for microchannels, Science 295 (5555) (2002) 647–651.

[2] M. D. Tarn, S. N. Sikora, G. C. Porter, D. O'Sullivan, M. Adams, T. F. Whale, A. D. Harrison, J. Vergara-Temprado, T. W. Wilson, J.-u. Shim, et al., The study of atmospheric ice-nucleating particles via microfluidically generated droplets, Microfluidics and Nanofluidics 22 (5) (2018) 52.

[3] T. Karayiannis, M. Mahmoud, Flow boiling in microchannels: Fundamentals and applications, Applied Thermal Engineering 115 (2017) 1372–1397.

[4] G. Agarwal, T. Kazior, T. Kenny, D. Weinstein, Modeling and analysis for thermal management in gallium nitride HEMTs using microfluidic cooling, Journal of Electronic Packaging 139 (1).

[5] A. F. Al-Neama, N. Kapur, J. Summers, H. M. Thompson, An experimental and numerical investigation of the use of liquid flow in serpentine microchannels for microelectronics cooling, Applied Thermal Engineering 116 (2017) 709–723.

[6] Y. Zhang, H.-R. Jiang, A review on continuous-flow microfluidic PCR in droplets: Advances, challenges and future, Analytica Chimica Acta 914 (2016) 7–16.

[7] X. Zhu, H. Modi, A. Ayala, J. Kilbane, Rapid detection and quantification of microbes related to microbiologically influenced corrosion using quantitative polymerase chain reaction, Corrosion 62 (11) (2006) 950–955.

[8] A. Agrawal, B. Lal, Rapid detection and quantification of bisulfite reductase genes in oil field samples using real-time PCR, FEMS Microbiology Ecology 69 (2) (2009) 301–312.

[9] J. Park, H. Park, Thermal cycling characteristics of a 3d-printed serpentine microchannel for DNA amplification by polymerase chain reaction, Sensors and Actuators A: Physical 268 (2017) 183–187.

[10] J. Lee, M. Lee, E. Kulla, A. Tripathi, The effect of dilution on the dispersion with respect to microfluidic channel geometries, International Journal of Heat and Mass Transfer 104 (2017) 813–818.

[11] J. Khandurina, T. E. McKnight, S. C. Jacobson, L. C. Waters, R. S. Foote, J. M. Ramsey, Integrated system for rapid pcr-based dna analysis in microfluidic devices, Analytical chemistry 72 (13) (2000) 2995–3000.

[12] M. U. Kopp, A. J. De Mello, A. Manz, Chemical amplification: continuous-flow PCR on a chip, Science 280 (5366) (1998) 1046–1048.

[13] S. Thomas, R. L. Orozco, T. Ameel, Thermal gradient continuous-flow PCR: a guide to design, Microfluidics and Nanofluidics 17 (6) (2014) 1039–1051.

[14] J. J. Chen, C. M. Shen, Y. W. Ko, Analytical study of a microfludic DNA amplification chip using water cooling effect, Biomedical Microdevices 15 (2) (2013) 261–278.

[15] P.-C. Chen, W. Fan, T.-K. Hoo, L. C. Z. Chan, Z. Wang, Simulation guided-design of a microfluidic thermal reactor for polymerase chain reaction, Chemical Engineering Research and Design 90 (5) (2012) 591–599.

[16] Q. Cao, M.-C. Kim, C. Klapperich, Plastic microfluidic chip for continuous-flow polymerase chain reaction: Simulations and experiments, Biotechnology journal 6 (2) (2011) 177–184.

[17] M. Hashimoto, P.-C. Chen, M. W. Mitchell, D. E. Nikitopoulos, S. A. Soper, M. C. Murphy, Rapid PCR in a continuous flow device, Lab on a Chip 4 (6) (2004) 638–645.

[18] Y. Schaerli, R. C. Wootton, T. Robinson, V. Stein, C. Dunsby, M. A. Neil, P. M. French, A. J. DeMello, C. Abell, F. Hollfelder, Continuous-flow polymerase chain reaction of single-copy dna in microfluidic microdroplets, Analytical chemistry 81 (1) (2009) 302–306.

[19] M. Mitchell, X. Liu, Y. Bejat, D. Nikitopoulos, S. Soper, M. Murphy, Microfluidics, biomems, and medical microsystems, Proc. SPIE–Int. Soc. Opt. Eng., San Jose, CA, USA.

[20] J. Chiou, P. Matsudaira, A. Sonin, D. Ehrlich, A closed-cycle capillary polymerase chain reaction machine, Analytical chemistry 73 (9) (2001) 2018–2021.

[21] O. Frey, S. Bonneick, A. Hierlemann, J. Lichtenberg, Autonomous microfluidic multi-channel chip for real-time pcr with integrated liquid handling, Biomedical Microdevices 9 (5) (2007) 711–718.

[22] V. Duryodhan, A. Singh, S. G. Singh, A. Agrawal, A simple and novel way of maintaining constant wall temperature in microdevices, Scientific Reports 6 (2016) 18230.

[23] L. Gui, C. L. Ren, Numeric simulation of heat transfer and electrokinetic flow in an electroosmosis-based continuous flow PCR chip, Analytical Chemistry 78 (17) (2006) 6215–6222.

[24] R. Kodzius, K. Xiao, J. Wu, X. Yi, X. Gong, I. G. Foulds, W. Wen, Inhibitory effect of common microfluidic materials on PCR outcome, Sensors and Actuators B: Chemical 161 (1) (2012) 349–358.

[25] Y. Zhang, P. Ozdemir, Microfluidic DNA amplification—a review, Analytica Chimica Acta 638 (2) (2009) 115–125.

[26] V. Miralles, A. Huerre, F. Malloggi, M.-C. Jullien, A review of heating and temperature control in microfluidic systems: techniques and applications, Diagnostics 3 (1) (2013) 33–67.

[27] S. Tsuda, H. Jaffery, D. Doran, M. Hezwani, P. J. Robbins, M. Yoshida, L. Cronin, Customizable 3d printed 'plug and play' millifluidic devices for programmable fluidics, PLoS One 10 (11).

[28] V. E. Papadopoulos, G. Kokkoris, I. N. Kefala, A. Tserepi, Comparison of continuous-flow and static-chamber $\mu$pcr devices through a computational study: the potential of flexible polymeric substrates, Microfluidics and Nanofluidics 19 (4) (2015) 867–882.

[29] Z. Khatir, H. Thompson, Cfd-enabled design optimisation of industrial flows–theory and practise (2019).
[30] S. Gur, T. Danielson, Q. Xiong, C. Hin, S. Pannala, G. Frantziskonis, A. Savara, C. S. Daw, Wavelet-based surrogate time series for multiscale simulation of heterogeneous catalysis, Chemical Engineering Science 144 (2016) 165–175.
[31] A. Serani, R. Pellegrini, J. Wackers, C.-E. Jeanson, P. Queutey, M. Visonneau, M. Diez, Adaptive multi-fidelity sampling for cfd-based optimisation via radial basis function metamodels, International Journal of Computational Fluid Dynamics 33 (6-7) (2019) 237–255.
[32] R. T. Haftka, D. Villanueva, A. Chaudhuri, Parallel surrogate-assisted global optimization with expensive functions–a survey, Structural and Multidisciplinary Optimization 54 (1) (2016) 3–13.
[33] C. González Niño, N. Kapur, M.-F. King, G. de Boer, A. J. Blacker, R. Bourne, H. Thompson, Computational fluid dynamic enabled design optimisation of miniaturised continuous oscillatory baffled reactors in chemical processing, International Journal of Computational Fluid Dynamics (2019) 1–15.
[34] D. Domingo, I. Malmierca-Vallet, L. Sime, J. Voss, E. Capron, Using ice cores and gaussian process emulation to recover changes in the greenland ice sheet during the last interglacial, Journal of Geophysical Research: Earth Surface 125 (5) (2020) e2019JF005237.
[35] E. C. Garrido-Merchán, D. Hernández-Lobato, Dealing with categorical and integer-valued variables in bayesian optimization with gaussian processes, Neurocomputing 380 (2020) 20–35.
[36] J.-X. Wang, J.-L. Wu, H. Xiao, Physics-informed machine learning approach for reconstructing reynolds stress modeling discrepancies based on dns data, Physical Review Fluids 2 (3) (2017) 034603.
[37] M. Kotinis, A. Kulkarni, Multi-objective shape optimization of transonic airfoil sections using swarm intelligence and surrogate models, Structural and Multidisciplinary Optimization 45 (5) (2012) 747–758.
[38] P.-C. Chen, D. E. Nikitopoulos, S. A. Soper, M. C. Murphy, Temperature distribution effects on micro-cfpcr performance, Biomedical Microdevices 10 (2) (2008) 141–152.
[39] D. Moschou, N. Vourdas, G. Kokkoris, G. Papadakis, J. Parthenios, S. Chatzandroulis, A. Tserepi, All-plastic, low-power, disposable, continuous-flow PCR chip with integrated microheaters for rapid DNA amplification, Sensors and Actuators B: Chemical 199 (2014) 470–478.
[40] I. Aziz, R. Jamshaid, T. Zaidiand, I. Akhtar, Numerical simulation of heat transfer to optimize DNA amplification in polymerase chain reaction, in: 2016 13th International Bhurban Conference on Applied Sciences and Technology (IBCAST), IEEE, 2016, pp. 456–462.
[41] D. T. Chiu, A. J. deMello, D. Di Carlo, P. S. Doyle, C. Hansen, R. M. Maceiczyk, R. C. Wootton, Small but perfectly formed? successes, challenges, and opportunities for microfluidics in the chemical and biological sciences, Chem 2 (2) (2017) 201–223.
[42] F. M. White, I. Corfield, Viscous fluid flow, Vol. 3, McGraw-Hill New York, 2006.
[43] B. Davaji, Thermal microfluidic devices; design, fabrication and applications.
[44] T. L. Bergman, F. P. Incropera, D. P. DeWitt, A. S. Lavine, Fundamentals of heat and mass transfer, John Wiley & Sons, 2011.
[45] W. Qu, I. Mudawar, Analysis of three-dimensional heat transfer in micro-channel heat sinks, International Journal of heat and mass transfer 45 (19) (2002) 3973–3985.
[46] J. J. Chen, M. H. Liao, K. T. Li, C. M. Shen, One-heater flow-through polymerase chain reaction device by heat pipes cooling, Biomicrofluidics 9 (1) (2015) 014107.
[47] J. Holman, Heat transfer, 10th dn (2009).
[48] Y. Cengel, Heat and mass transfer: fundamentals and applications, McGraw-Hill Higher Education, 2014.
[49] R. Shah, A correlation for laminar hydrodynamic entry length solutions for circular and noncircular ducts.
[50] B. Xu, P.-W. Li, C. L. Chan, Extending the validity of lumped capacitance method for large biot number in thermal storage application, Solar Energy 86 (6) (2012) 1709–1724.
[51] V. Ranmode, M. Singh, J. Bhattacharya, Analytical formulation of effective heat transfer coefficient and extension of lumped capacitance method to simplify the analysis of packed bed storage systems, Solar Energy 183 (2019) 606–618.
[52] J.-R. Lin, C.-M. Wu, T.-M. Liou, C.-Y. Huang, The study of axial heat conduction with various

hydraulic diameters of microchannel, Procedia Engineering 79 (2014) 273–278.

[53] G. Maranzana, I. Perry, D. Maillet, Mini-and micro-channels: influence of axial conduction in the walls, International journal of heat and mass transfer 47 (17-18) (2004) 3993–4004.

[54] A. Narayanan, V. Toropov, A. Wood, I. Campean, Simultaneous model building and validation with uniform designs of experiments, Engineering Optimization 39 (5) (2007) 497–512.